Sensors and Materials, Vol. 37, No. 4 (2025) 1579–1590
MYU Tokyo

S & M 4006

Comparative Analysis of Distribution-based Ground Truth Designs for Enhanced Accuracy in Bleeding Alert Map

Takugo Osakabe,† Niran Nataraj,† Maina Sogabe,* and Kenji Kawashima

Graduate School of Information Science and Technology, The University of Tokyo,
Hongo Campus, 7-3-1 Hongo, Bunkyo-ku, Tokyo 113-8656, Japan

(Received December 17, 2024; accepted March 21, 2025)

Keywords: medical imaging, generative adversarial network, image-to-image translation, surgical robotics, Bleeding Alert Map (BAM)

Accurately identifying bleeding sources during minimally invasive surgery (MIS) is crucial for patient safety, faster discharge, and reducing operative time and postoperative complications. Although advances in imaging and bleeding segmentation have improved detection, pinpointing precise hemorrhage origins remains challenging owing to high variability in surgical environments. To address this, Bleeding Alert Maps (BAMs) were initially generated using a fixed Gaussian distribution; however, this static assumption was insufficient to capture the full range of bleeding variability. In this study, we systematically investigate kurtosis as a key factor in BAM construction, evaluating uniform (low kurtosis), Gaussian (moderate kurtosis), and exponential (high kurtosis) ground truth distributions. We apply a generative adversarial network (GAN) to produce BAMs from these distributions, each tested across multiple spread parameters (σ for Gaussian and s for exponential). Our results show that while Gaussian-distribution-based BAMs improve up to $\sigma \approx 40$ and then plateau, exponential-distribution-based BAMs continue to yield accuracy gains beyond this threshold, demonstrating a clear distributional advantage. Notably, the best exponential model ($s = 50$) achieved a ~92% bleeding-point detection rate (137 true positives out of 150), ~85% accuracy, 88% precision, and an F1 score of 0.898. These findings underscore how refining the distribution shape, particularly increasing its kurtosis, significantly enhances the reliability, applicability, and clinical value of automated bleeding source localization in MIS.

1. Introduction

Minimally invasive surgeries (MISs), including endoscopic procedures, are increasingly adopted across various specialties—abdominal, thoracic,[1] pelvic, and breast[2]—owing to improved patient recovery and reduced complications.[3] However, endoscopic surgeries introduce risks not encountered in open surgeries. Intraoperative bleeding is a critical determinant influencing patient prognosis during these procedures.[4] While inserting an endoscopic camera and forceps into the abdominal or thoracic cavity enables the removal of

*Corresponding author: e-mail: fsogabe-vet@g.ecc.u-tokyo.ac.jp
†Equal Contribution
https://doi.org/10.18494/SAM5507

ISSN 0914-4935
https://myukk.org/

lesions such as tumors without making large incisions, it also presents distinct challenges.[5] The narrow, limited field of view increases the likelihood of instrument interference, and because of this restricted visibility, there is a considerable risk of damaging organs beyond the visual field or at its periphery. Bleeding can further reduce visibility, complicating the procedure.[6,7] Additionally, the limited number of instruments that can be introduced restricts the methods available for managing bleeding.[8,9] Consequently, locating the origin of bleeding—the site requiring hemostasis—is often difficult. As a result, the patient's blood volume may not be maintained, leading to worsened postoperative recovery and potential complications. In such cases, surgeons may ultimately need to convert to open abdominal or thoracic surgery, increasing the patient's burden.

Thus, several systems for bleeding recognition were proposed in previous studies. For example, Okamoto *et al.*[10] proposed a real-time method for segmented blood regions to support hemostasis during laparoscopic surgery. Jiang *et al.*[11] developed an AI system that uses bounding boxes to indicate bleeding areas. While these methods accurately estimate bleeding regions, they do not provide information about the specific sites where hemostasis is needed. This limitation arises as obtaining precise information about the bleeding origin is challenging. Chang *et al.*[12] introduced a method using particle swarm analysis and García-Martinez *et al.*[13] introduced a method using computer vision to estimate bleeding sources; however, introducing these previous approaches for precise bleeding point detection is difficult. In a recent study, a multitask convolutional neural network (CNN) was applied in a BLAIR system[14] for bleeding detection in robotic prostatectomy, using semantic segmentation and classification to detect blood accumulation, but it lacks precise localization of bleeding origins and only provides regional alerts rather than pinpoint accuracy. Similarly, Hua *et al.* [15] employed a Faster R-CNN with optical flow analysis for bleeding detection in laparoscopic surgery, but their approach is constrained to bounding-box-based segmentation, making it incapable of identifying exact bleeding points or differentiating between minor and critical hemorrhages.

In response, Sogabe *et al.*[16] proposed a new method called the Bleeding Alert Map (BAM) for estimating bleeding origin information using the generative adversarial network (GAN)-based method. This technique employs a silicone-based data acquisition device known as a mimic organ system to obtain both bleeding origin information and images during bleeding. By formulating this information as a dataset, they enabled an AI system to learn the relationship between accurate bleeding point coordinates and bleeding image information. Recognizing that navigating surgeons towards the bleeding point using only the point information could lead to unexpected hazards owing to reasons such as AI prediction failures, surgical errors, or positional deviations caused by patient movement, they proposed presenting the bleeding origin information as an alert map. This map indicates the risk level of the bleeding origin's presence, enhancing safety during practical applications.

The initial heat map was generated by assuming a normal distribution centered at the bleeding origin. However, issues arose regarding this approach because areas with a high likelihood of bleeding are not expected to follow a normal distribution, exposing a limitation in the previous work. Therefore, in this study, we aim to improve the accuracy of the BAM by verifying the BAM framework using various model-based ground truths (GTs) of alert map

information. We will examine the optimal distribution and its parameter design for this GT information to enhance the precision of the BAM system.

The selection of an appropriate distribution for generating GT data in alert maps is critical for accurately capturing the spatial characteristics of bleeding risk during endoscopic surgery. The normal distribution[17] is one of the most widely used statistical models for representing spatial data, owing to its simplicity and symmetric properties. In the context of alert maps, it is assumed that risk levels decrease symmetrically with distance from the bleeding point. This model is computationally efficient and serves as a baseline for comparison with more complex approaches. The exponential distribution models the time or distance between discrete events,[18] such as the interval between two bleeding points. This model is useful for sequential risk assessments or predicting the proximity of bleeding events to specific locations.

In this study, the above-mentioned distribution models are employed as representation methods to evaluate the effect of kurtosis differences on BAM accuracy. By systematically varying their respective parameters, we identify the ground truth configuration that most precisely delineates the bleeding source. Ultimately, this approach aims to enhance the precision of the BAM-based navigation system, thereby contributing to the development of a safer and more effective surgical navigation framework. We hypothesize that the kurtosis of the latent distribution significantly influences the quality of GAN-based BAM generation

2. Data, Materials, and Methods

2.1 Dataset

The dataset used in this study was derived from the mimic organ dataset by Sogabe *et al.*[16] To more closely replicate intraoperative bleeding conditions, this dataset was generated using a simulated vascular perfusion system. It comprises a 3% agar layer to mimic soft tissue, within which silicone tubing (3–5 mm in diameter) is embedded to represent blood vessels. Blood flow is regulated by a peristaltic pump (MP-3N, Eyela Tokyo Rikakikai Co., Ltd., Japan) at a controlled rate of 0.3–0.5 mm/s. In addition, to capture a wide range of hemorrhagic events, bleeding was induced using a precisely controlled 18G needle. The needle punctured the vessel surfaces at varying angles, thereby simulating diverse severities of vascular injury, from capillary-level microbleeds to arterial-scale hemorrhages.

Figure 1 illustrates one of the images included in the dataset. From 200 different video scenes, 3000 images from 150 scenes were used as the training data, and 200 images extracted from 50 scenes were used as the test data. Both sets comprised 75% images with bleeding occurring and 25% images without any bleeding. To ensure a fair comparison of the alert map performance, the same data augmentation methods were applied across all groups. The data augmentation included scaling (0.72 to 1.5), cropping, and rotation (−180° to +180°).

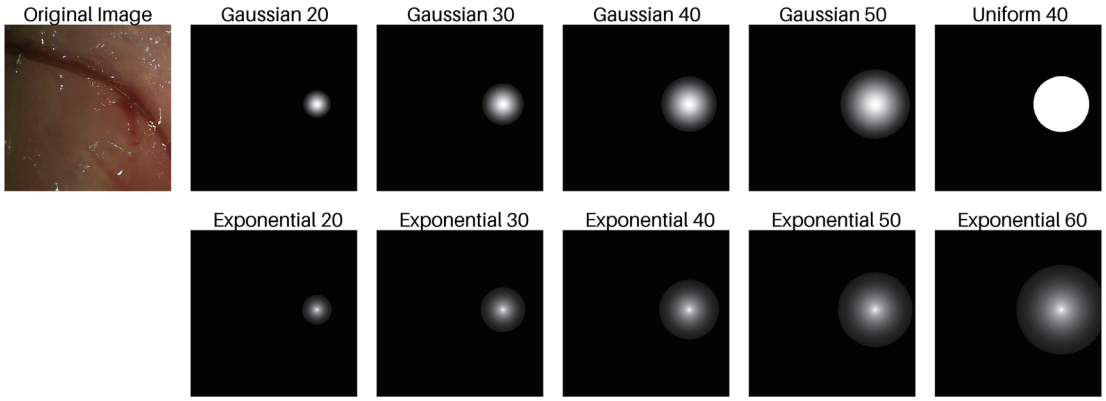

Fig. 1. (Color online) Distributions for GT BAMs. BAMs are generated on the basis of the original image. BAMs on the upper row were generated based on Gaussian and uniform distribution, and those on the lower row were generated based on exponential distribution. The parameter σ or s becomes larger in images further to the right.

2.2 GT map

Formulas for Gaussian (1), exponential (2) and uniform distributions are provided below.

$$f\left(x,\mu,\Sigma\right)=\exp\left(-\frac{1}{2}\left(x-\mu\right)^{T}\Sigma^{-1}\left(x-\mu\right)\right)\ \text{where}\ \Sigma=\sigma^{2}I \tag{1}$$

$$f\left(x,\mu,s\right)=\exp\left(-\frac{d\left(x,\mu\right)}{s}\right)\ \text{where}\ d\left(x,\mu\right)=\sqrt{\left\|x-\mu\right\|^{2}} \tag{2}$$

μ represents the coordinates of the bleeding point in Eqs. (1) and (2) above. Three types of BAM distribution represent different kurtosis levels: uniform distribution is an example of platykurtic distribution with a nearly flat profile, Gaussian distribution is the conventional mesokurtic distribution used in prior work,[16] and exponential distribution represents a leptokurtic distribution characterized by a sharp peak at the bleeding point and heavier tails.

We conducted evaluations using 10 different patterns by varying the parameters as specified in Table 1. The intensity threshold is set to 0.1 because it is meaningless if the intensity is too small when estimating the bleeding point based on BAMs. Uniform BAMs were generated by replacing all intensity values greater than 0.1 in Gaussian distributions ($\sigma = 40$) with 1.0. Figure 1 shows the distribution method used for BAM in this study, along with the GT alert map generated by this method.

Table 1
Threshold and bleeding point coordinate parameters for Gaussian and exponential distributions.

Distribution	μ	$\sigma \mid s$	Threshold
Uniform	Bleeding Point Coordinate	{40}	0.1
Gaussian	Bleeding Point Coordinate	{20, 30, 40, 50}	0.1
Exponential	Bleeding Point Coordinate	{20, 30, 40, 50, 60}	0.1

2.3 BAM generation

The whole BAM generation system structure is shown in Fig. 2. The BAM generation AI was developed by refining previous frameworks and utilizing the Pix2PixHD architecture,[19] a high-resolution conditional GAN designed for image-to-image translation tasks. Compared with Pix2Pix,[20] Pix2PixHD incorporates a multiscale generator and multiple discriminators, enabling higher-resolution outputs (e.g., 512 × 512) and better handling of fine-grained details. In this setup, bleeding scene images are input into the generator trained to produce the corresponding BAMs. Adversarial learning, facilitated by multiscale discriminators, ensures spatial coherence and reliability, enhancing the accuracy and quality of the generated BAMs. Previous reliable studies show Pix2PixHD strengths in medical use with accurate predictions and better correlative learning.[21–23]

All training parameters were carefully selected to balance computational feasibility, model stability, and output quality. We employed the same configuration across all training, with an initial learning rate of 3×10^{-5} and a batch size of 5, and the model was trained for a total of 200 epochs to ensure the progressive refinement of the generated BAMs. Both input and output resolutions were maintained at 512 × 512 to support detailed feature representation. Feature-matching losses were introduced to enhance perceptual fidelity, and instance normalization provided stable training conditions. A multiscale discriminator enabled comprehensive spatial discrimination, while the chosen number of generator and discriminator filters ensured a practical balance between model complexity and training efficiency.

2.4 Evaluation

The evaluation was conducted using 200 data samples (150 bleeding and 50 nonbleeding images) from scenes that were not included in the training set. For each sample, the presence or absence of BAM generation within the correct bleeding onset coordinates and other areas were examined. Key metrics such as accuracy rate (AR), recall rate (RR), precision rate (PR), and other related parameters were calculated using the following equations:

$$AR = \frac{TP + TN}{TP + FP + TN + FN}, RR = \frac{TP}{TP + FN}, PR = \frac{TP}{TP + FP}, \tag{3}$$

where TP, FP, TN, and FN represent the numbers of true positives, false positives, true negatives, and false negatives, respectively. Additionally, for 150 images where bleeding occurred, the

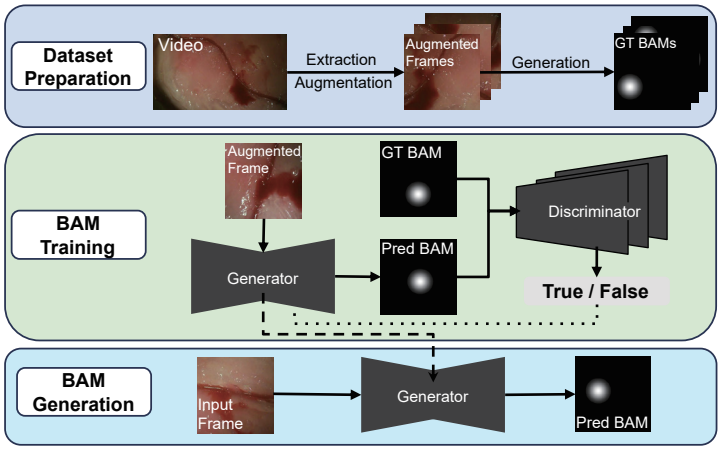

Fig. 2. (Color online) Framework overview showing dataset preparation, GAN-based training, and inference stages for Bleeding Attention Map (BAM) generation, highlighting Ground Truth (GT) and Predicted (Pred) BAM outputs for real-time surgical bleeding localization.

variation was analyzed on the basis of two criteria: whether the generated BAM exists and covers the bleeding points and the ratio of overlapping area between the GT alert maps and the generated BAMs (Fig. 3). The threshold here for the overlapping ratio was set to 50%. The indicators Correct Alert Rate (CAR) and Incorrect Alert Rate (ICAR) are also calculated.[16]

2.5 Experiments

The comparison of the evaluated results was conducted in two ways, kurtosis comparison and parameter comparison. In the kurtosis comparison, the accuracy of the generated BAMs was compared, and three types of distributions, uniform, Gaussian and exponential distributions, were utilized. The parameter was set to 40 for all distributions to make the BAM size almost the same as the BAM size used in the research by Sogabe *et al.*[16] In the parameter comparison, referring to the results of kurtosis comparison, two types of distributions, Gaussian and exponential, were used with different parameters.

3. Results

3.1 Kurtosis comparison

Figure 4(a) presents a few examples of GAN-generated BAMs, while exponential (leptokurtic) distribution showed sufficient performance, and uniform (platykurtic) distribution generated BAM at a position away from the bleeding point. Figure 4(b) shows that AR rates improved as the distribution became steeper: 0.485 in uniform distribution and 0.795 in exponential distribution.

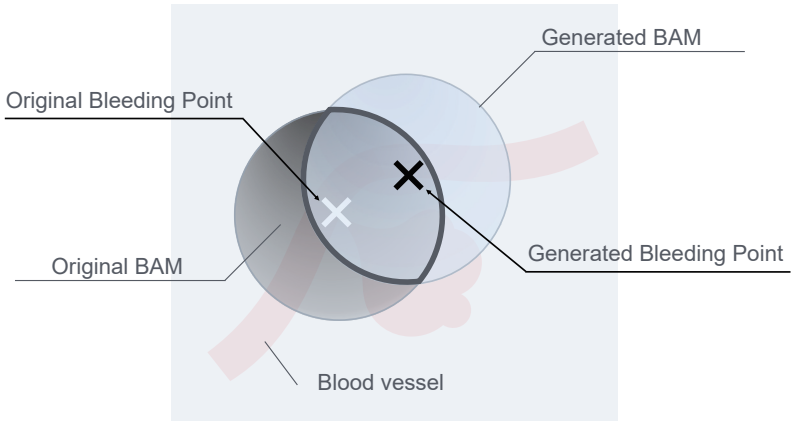

Fig. 3. (Color online) Original GT BAM and the generated BAM, highlighting the overlapping regions. The bleeding origin is indicated by "X". The degree of overlap is utilized to evaluate the BAM model's performance.

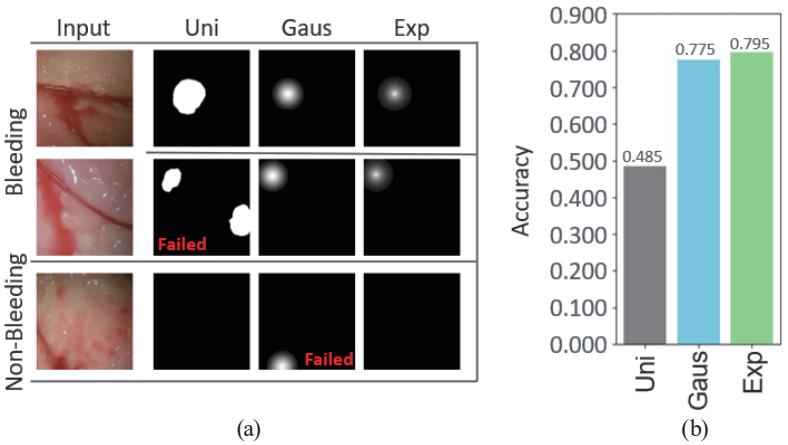

Fig. 4. (Color online) (a) Examples of generated BAMs and (b) accuracy of generated BAM for three distributions.

3.2 Parameter comparison

3.2.1 Generated BAMs

Figure 5 shows examples of BAMs generated by GANs. The leftmost example illustrates a GAN-generated BAM with sufficient performance. BAMs with larger s-parameter values, especially exponential distributions with s = 40 and 50, demonstrated better performance than the smaller parameter cases, accurately capturing the bleeding regions in all listed examples.

Table 2 shows that both Gaussian and exponential distributions benefit from increasing BAM size, although their performance trajectories differ. Gaussian models exhibit early improvements:

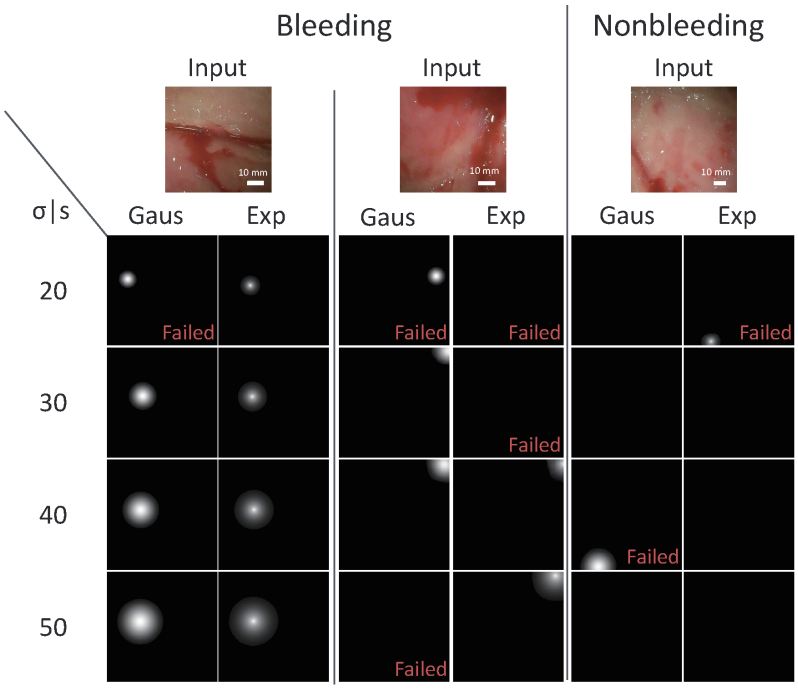

Fig. 5. (Color online) BAMs generated by GANs from the input images.

Table 2
Performance metrics for Gaussian and exponential distributions across varying parameters.

Distribution	$\sigma\|s$	CAR	ICAR	TP	FN	FP	TN	AR	RR	PR	F1
Gaussian	20	0.377	0.008	65	85	12	38	0.515	0.433	0.844	0.573
	30	0.630	0.013	105	45	12	38	0.715	0.700	0.897	0.787
	40	0.744	0.021	127	23	22	28	0.775	0.847	0.852	0.849
	50	0.736	0.035	125	25	25	25	0.750	0.833	0.833	0.833
Exponential	20	0.497	0.008	86	64	17	33	0.595	0.573	0.835	0.680
	30	0.637	0.012	108	42	10	40	0.740	0.720	0.915	0.806
	40	0.713	0.017	123	27	14	36	0.795	0.820	0.898	0.857
	50	0.783	0.029	137	13	18	32	0.845	0.913	0.884	0.898
	60	0.787	0.047	131	19	20	30	0.805	0.873	0.868	0.870

F1 rises from 0.573 at $\sigma = 20$ to 0.849 at $\sigma = 40$ (~48% increase), but plateaus by $\sigma = 50$, indicated by a slight drop in TP (127 to 125) and a decrease in F1 (0.833 from 0.849). Conversely, exponential models sustain progress more consistently: between $s = 20$ and $s = 40$, F1 increases from 0.680 to 0.857 (~26% gain), and at $s = 50$, both TP and F1 continue to improve (TP from 123 to 137 and F1 from 0.857 to 0.898), demonstrating persistent benefits at larger scales.

3.2.2 Accuracy of generated BAMs

Figure 6, for which we employed row normalization for clearer comparison, illustrates the effect of varying the BAM size on TP detection. For Gaussian distribution, TP rises from 43% at

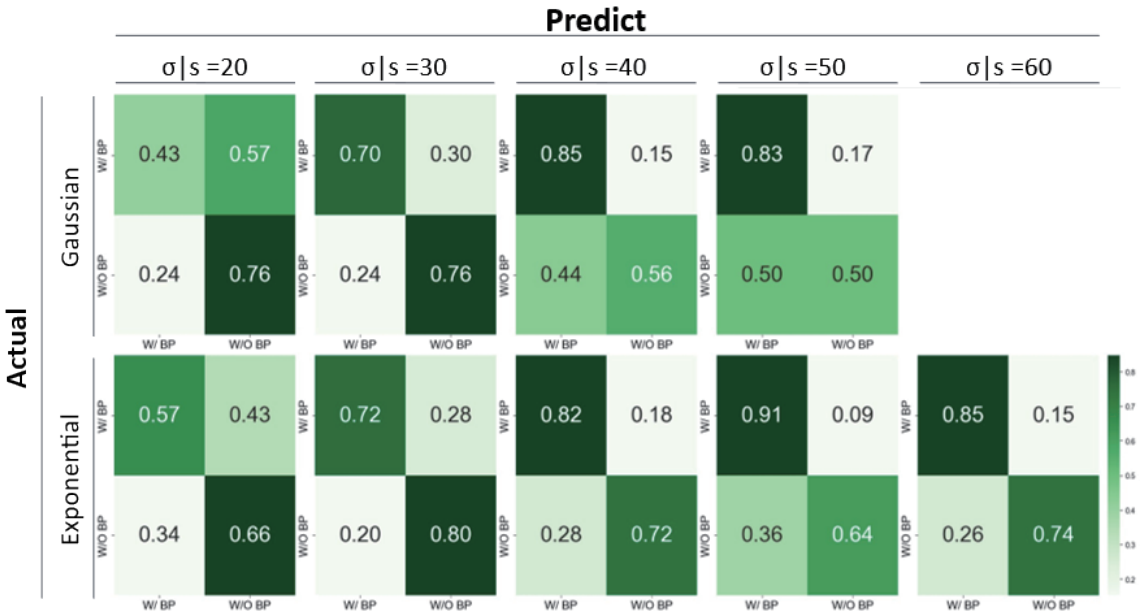

Fig. 6. (Color online) Row-normalized confusion matrices for comparing for Gaussian and exponential methods across sigma values for classification performance analysis.

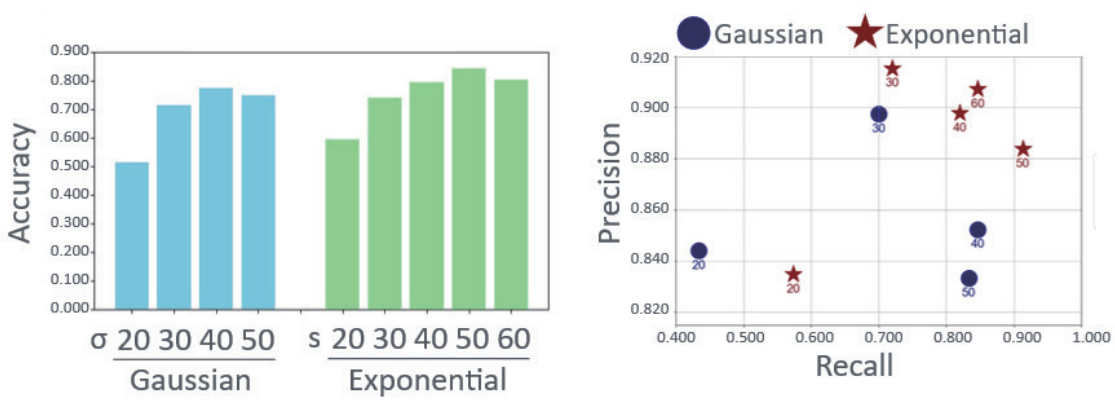

(a) (b)

Fig. 7. (Color online) (a) Accuracy rate and (b) precision vs recall graph for $\sigma|s$ values of the two distributions.

σ = 20 to 83% at σ = 50, and for exponential distribution, from 57% at s = 20 to 91% at s = 50. This confirms a strong proportional dependence on BAM size, as larger BAMs generally yield higher TP ratios. Although increasing σ or s may slightly raise the FP ratio for most configurations, the Gaussian distribution at σ = 50 notably does not exhibit this FP increase, marking a unique exception.

Figure 7(a) shows that AR and TP rates improve with larger BAM sizes. While Gaussian distribution saturates beyond σ = 40, consistent with insights gained from accuracy data and the confusion matrix, exponential distributions display a more sustained, nearly logarithmic growth in both AR and TP, maintaining a positive learning trajectory even beyond s = 40. In the case of

exponential distribution with $s = 60$, the AR rate dropped, showing a similar pattern to Gaussian distribution.

Figure 7(b) enables another layer of understanding by examining precision and recall. Both distributions achieve higher recall as σ or s increases, reflecting enhanced detection capabilities. However, the precision gains of Gaussian distribution stall and decrease at higher σ, meaning that further improvements in recall do not translate into notable precision increases. Exponential distributions, on the other hand, not only preserve higher recall at larger s values but also maintain or improve precision, which is clearly visible in the graph. This balanced progression enables exponential models to approach a more optimal precision–recall combination at larger scales.

4. Discussion

The results of the kurtosis comparison indicate that a steeper distribution is a better option for GT of GAN generation of BAMs. Additionally, the results of the parameter comparison confirm that larger BAM sizes generally improve model performance. Initially, it was anticipated that increasing BAM coverage would raise accuracy and TP rates since a larger mask can encompass more potential bleeding areas. While Gaussian-distribution-based models achieve substantial early gains, their σ-performance plateaus around $\sigma = 40$ to 50, due in part to broad high-intensity regions that do not necessarily correspond to actual bleeding sources. This saturation explains why Gaussian distribution with $\sigma = 40$ outperforms that with $\sigma = 50$ in some metrics, since enlarging the BAM further disperses the model's focus without offering precise location cues.

In contrast, the exponential distribution leverages its intensity decay to progressively refine spatial focus. The incremental improvements in CAR and ICAR under exponential distribution conditions signify that as the model grows, it becomes better at distinguishing crucial bleeding regions from irrelevant areas. The stable improvements noted in both accuracy and the precision–recall balance highlight the exponential distribution's capacity for sustained learning, even as s surpasses thresholds where Gaussian-distribution-based models stagnate. However, like the Gaussian-distribution-based model, the accuracy plateaus after $s = 50$, strengthening our observation that larger BAMs lead to false attention to nonbleeding areas. This difference in behavior underscores the importance of distribution choice: exponential-distribution-based BAMs continue to enhance detection accuracy and maintain an advantageous precision–recall profile at larger scales, effectively pushing the precision–recall frontier outward.

This study has several limitations. First, only two types of distribution, Gaussian and exponential, were examined. While effective, this limited scope may restrict the model's ability to generalize to some surgical environments. Additionally, although the model did use color images as input, allowing it to learn some color-based features indirectly through its feature layers, explicit methods to leverage color and texture information were not implemented. In future research, advanced techniques might be explored, such as explicit color segmentation or multimodal input integration, to enhance the model's ability to distinguish bleeding and nonbleeding regions. Furthermore, investigating more complex, nonuniform distributions like

anisotropic Gaussian or Poisson models could provide deeper insights into optimizing BAM generation for various surgical scenarios. Among the tested configurations, the exponential distribution with $s = 50$ yielded the best overall performance, achieving the highest recall (0.913) and F1 score (0.898). This result underscores the advantage of larger BAMs in covering bleeding regions and enhancing detection sensitivity. However, when s is 50, the configuration introduced challenges, such as increased overlap with nonbleeding areas, which could reduce precision and create visual clutter in surgical applications. In contrast, the BAM whose s is set to 40 offered a more compact representation, maintaining high recall (0.820) and precision (0.898). This makes $s = 40$ a more balanced and practical choice for real-world usage in effectively localizing bleeding points while minimizing unnecessary distractions.

Moving beyond accuracy metrics, the visibility and usability of BAMs from a surgeon's perspective are critical for practical implementation. Effective surgical navigation requires BAMs that integrate seamlessly without causing visual or cognitive overload. Future research could be focused on refining BAM designs to balance sensitivity, precision, and usability more effectively. Adaptive BAM configurations that dynamically adjust their size in accordance with the surgical context or user preferences could address these issues. Additionally, incorporating user-end parameters, such as the type of surgery and surgeon expertise, will be crucial for tailoring the BAM system to diverse clinical scenarios.

5. Conclusions

Our approach uniquely leverages the impact of distribution kurtosis on GAN performance, moving beyond traditional static Gaussian distribution assumptions, to systematically optimize GT designs for BAM generation. This innovation refines spatial accuracy and provides a robust framework for tailoring surgical navigation systems, setting our work apart from previous studies. In this study, we compared distribution-based GT designs for BAM generation, demonstrating their significant impact on GAN-driven bleeding localization. Our results indicate that a more sharply peaked distribution yields more effective BAMs: an exponential distribution with $s = 40$ provides a balanced performance by maintaining high recall and precision while minimizing overlap with nonbleeding regions, whereas a larger exponential BAM ($s = 50$) offers superior sensitivity but introduces challenges in precision and usability. Overall, exponential BAM models outperformed their Gaussian counterparts; notably, the best exponential model ($s = 50$) achieved a bleeding point detection rate of ~92% (137 TP out of 150), with ~85% accuracy, 89% precision, and an F1 score of 0.898. These outcomes underscore the importance of GT distribution design in enhancing bleeding source detection in MIS and contribute to the development of safer, more efficient surgical navigation systems. Future research could include refining this framework by incorporating surgeon feedback, exploring more complex distribution models, and adapting BAM parameters to specific surgical scenarios, ultimately evolving the approach into a robust tool for real-world clinical applications.

Acknowledgments

This work was supported by JST, ACT-X Grant Number JPMJAX23CC, Japan.

References

1 M. Lijster, R. Bergevoet, E. Dalen, E. Michiels, H. Caron, L. Kremer, and D. Aronson: Cochrane Database Syst. Rev. **1** (2012) CD008403. https://doi.org/10.1002/14651858.CD008403.pub2
2 S. Bromberg, P. Figueiredo, and F. Ades: Breast **44** (2019) S112. https://doi.org/10.1016/S0960-9776(19)30379-0
3 K. Mohiuddin and S. Swanson: J. Surg. Oncol. **108** (2013) 315. https://doi.org/10.1002/jso.23398
4 V. Martin-Gorgojo, S. Girona, and S. Donat: Revista Española de Cirugía Ortopédica y Traumatología **68** (2022) 322. https://doi.org/10.21203/rs.3.rs-1319710/v1
5 A. Avinash: A stereoscopic "pickup" camera for the da Vinci surgical system. (2020). https://doi.org/10.14288/1.0388490
6 D. Činčikas, J. Ivaškevičius, J. Martinkėnas, and S. Balseris: Medicina **46** (2010) 730. https://doi.org/10.3390/MEDICINA46110103
7 A. Medievsky, A. Zotin, K. Simonov, and A. Kruglyakov: Medicina i Vysokie Tehnologii (2022). https://doi.org/10.34219/2306-3645-2022-12-3-37-42
8 S.-J. Gao and M. J. Lee: Surgical Workflow Anticipation (2022). https://api.semanticscholar.org/CorpusID:259923345
9 M. Schäfer, M. Lauper, and L. Krähenbühl: Am. J. Surg. **180** (2000) 73. https://doi.org/10.1016/S0002-9610(00)00416-5
10 T. Okamoto, T. Ohnishi, H. Kawahira, O. Dergachyava, P. Jannin, and H. Haneishi: Signal, Image Video Process. **13** (2019) 405. https://doi.org/10.1007/s11760-018-1369-7
11 J. Jiang, Y. Lu, and S. Hua: ICGIP **11720** (2020) 117200C. https://doi.org/10.1117/12.2589338
12 K. Chang, J. Libertini, and S. Seay: J. Sci. Comput. **81** (2019) 1567. https://doi.org/10.1007/s10915-019-01099-7
13 Á, García-Martínez, J. Vicente-Samper, and J. Sabater-Navarro: Artif. Intell. Med. **78** (2017) 55. https://doi.org/10.1016/j.artmed.2017.06.002
14 E. Checcucci, P. Piazzolla, G. Marullo, C. Innocente, F. Salerno, L. Ulrich, S. Moos, A. Quarà, G. Volpi, D. Amparore, and F. Piramide: J. Clin. Med. **12** (2023) 7355. https://doi.org/10.3390/jcm12237355
15 S. Hua, J. Gao, Z. Wang, P. Yeerkenbieke, J. Li, J. Wang, G. He, J. Jiang, Y. Lu, Q. Yu, and X. Han: Ann. Transl. Med. **10** (2022). https://doi.org/10.21037/atm-22-1914
16 M. Sogabe, K. Ishikawa, T. Takamatsu, K. Takeuchi, T. Kanno, K. Fujimoto, T. Miyazaki, T. Kawase, T. Sato, and K. Kawashima: Array **19** (2023) 100308. https://doi.org/10.1016/j.array.2023.100308
17 C. M. Bishop: Pattern Recognition and Machine Learning (Springer, 2006). https://link.springer.com/book/9780387310732
18 S. M. Ross: Introduction to Probability Models (Academic Press, 2014). https://doi.org/10.1016/C2012-0-03564-8
19 T. C. Wang, M. Y. Liu, J. Y. Zhu, A. Tao, J. Kautz, and B. Catanzaro: Proc. IEEE Conf. Computer Vision and Pattern Recognition (2018) 8798–8807. https://doi.org/10.1109/CVPR.2018.00917
20 P. Isola, J. Y. Zhu, T. Zhou, and A. A. Efros: Proc. IEEE Conf. Computer Vision and Pattern Recognition (2017) 1125–1134.
21 F. Xu, X. Yu, Y. Gao, X. Ning, Z. Huang, M. Wei, W. Zhai, R. Zhang, S. Wang, and J. Li: Front. Bioeng. Biotechnol. **10** (2022) 1. https://doi.org/10.3389/fbioe.2022.914964
22 D. Jin, H. Zheng, Q. Zhao, C. Wang, M. Zhang, and H. Yuan: Tomography **7** (2021) 767. https://doi.org/10.3390/tomography7040064
23 A. Aljohani and N. Alharbe: Electronics **11** (2022) 3470. https://doi.org/10.3390/electronics11213470.